Plasma-enhanced atomic layer deposition of tungsten oxide thin films using (tBuN)2(Me2N)2W and O2 plasma

Plasma-enhanced atomic layer deposition of tungsten oxide thin films using (^{t}BuN)$_2$(Me$_2$N)$_2$W and O_2 plasma

Running title: Atomic layer deposition of tungsten oxide

Running Authors: Balasubramanyam et al

Shashank Balasubramanyam[1, a)], Akhil Sharma[1], Vincent Vandalon[1], H.C.M.Knoops[1, 2], W.M.M. (Erwin) Kessels[1], Ageeth A.Bol[1]

[1]Department of Applied Physics, Eindhoven University of Technology, P.O Box 513, 5600 MB Eindhoven, The Netherlands.

[2]Oxford Instruments Plasma Technology, North end, Bristol, BS49 4AP, United Kingdom

[a)] Electronic mail: s.balasubramanyam@tue.nl

The growth of tungsten oxide (WO_3) thin films by atomic layer deposition (ALD) offers numerous merits including atomic-scale thickness control at low deposition temperatures. In this work, we have developed and characterized a new plasma-enhanced ALD process for WO_3 thin films using the metalorganic precursor (^{t}BuN)$_2$(Me$_2$N)$_2$W and O_2 plasma as co-reactant over a wide temperature range of 100 °C-400 °C. The influence of deposition temperature on the growth behaviour and film properties is investigated in detail. The WO_3 ALD process developed in this work yields a relatively high growth per cycle (GPC) which varies from ~0.7 Å at 100 °C to ~0.45 Å at 400 °C, as-determined by in-situ spectroscopic ellipsometry (SE). Rutherford backscattering spectrometry (RBS) measurements revealed a mass density of 5.9 g/cm^3 and near stoichiometric film composition (O/W = 2.9). Both RBS and X-ray photoelectron spectroscopy (XPS) measurements confirmed no detectable C as well as N impurity incorporation. Grazing

incidence X-ray diffraction (GI-XRD) measurements indicated that the films deposited at 400 °C were polycrystalline in nature.

I. INTRODUCTION

Transition metal oxides exhibit interesting electrical, optical, and mechanical properties which classifies them as multi-functional for several applications. Amongst them, tungsten oxide (WO_3) has been of particular interest for electrochromic,[1–4] gas-sensing,[5,6] and catalytic[7,8] applications. In particular, WO_3 is extensively studied for electrochromic applications such as smart windows for automobiles and buildings.[9,10] Electrochromic WO_3 based auto-dimming rear view mirrors for automobiles are commercially available.[11] Recently, WO_3 thin films (i.e., having 5 nm-10 nm thickness) have attracted interest as a highly transparent hole-selective contact for c-Si solar cells.[12,13,14] Furthermore, WO_3 is being utilized in the synthesis of two-dimensional transition metal dichalcogenide (2D-TMD) such as tungsten disulfide (WS_2) through sulfurization of the oxide.[15,16] The application of WO_3 thin films for solar cells and 2D-TMD synthesis are particularly gaining a lot of interest lately.

WO_3 has been previously deposited using a wide range of deposition techniques including evaporation,[17,18] sputtering,[19,20] sol-gel deposition,[21,22] chemical vapour deposition (CVD),[23,24] and atomic layer deposition (ALD).[16,25–31] Growth of thin films via ALD has gained increasing popularity over the last few decades because of its ability to deposit ultra-thin uniform films with precise thickness control and its low temperature growth possibility. These merits of ALD are particularly valuable for the application of WO_3 thin films for solar cells and 2D-TMD synthesis. However, there are only a few

reports on ALD of WO_3 in the literature. Tägtström *et al.* have reported a WO_3 ALD process using in-situ-generated oxyfluorides as precursor and H_2O as co-reactant.[25] However, controlling the in-situ generated oxyfluoride species was difficult. Dezelah *et al.* utilized a metalorganic precursor $W_2(NMe_2)_6$ and H_2O in an ALD process which resulted in W_2O_3 films with trivalent tungsten, instead of WO_3.[26] Malm *et al.*[27] and *Nandi et al.*[28] investigated the ALD growth of WO_3 using the hexacarbonyl precursor $W(CO)_6$ and O_3. This process was characterized by relatively low growth per cycle (GPC) values of ~0.2 Å for temperatures below 250 °C and for temperatures above 250 °C the precursor decomposes thermally which leads to carbon impurity incorporation in the films.[27] Furthermore, an initial incubation delay of around 200 ALD cycles was reported.[27] *Mamun et al.*[29] and *Zhang et al.*[30] have also reported a GPC of 0.2 Å using the same hexacarbonyl precursor $W(CO)_6$ and H_2O. Recently, Song *et al.* utilized a plasma-based ALD process for WO_3 using $WH_2(iPrCp)_2$ and O_2 plasma, in their attempt to synthesis 2D-WS_2 nanosheets by sulfurizing WO_3 layers.[16] Their WO_3 ALD process yielded a high GPC of ~0.9 Å at 300 °C with the formation of sub-stoichiometric tungsten oxide (O/W = 2.4). The metalorganic precursor $(^tBuN)_2(Me_2N)_2W$ used in this work has been previously used by Liu *et al.* to deposit WO_3 by ALD using H_2O as co-reactant.[8] This process offers a high GPC of ~1 Å at 350 °C but relatively small GPC values (<0.2 Å) were observed for temperatures below 300 °C. From these literature reports it is evident that there is interest to develop a WO_3 ALD process with all of the following attributes: (1) high GPC (>0.2 Å), (2) low impurity incorporation, (3) wide temperature window, and (4) stoichiometric film composition (WO_3).

In this study, we report a plasma-enhanced ALD process for tungsten oxide thin films using $(^tBuN)_2(Me_2N)_2W$ and O_2 plasma over a wide temperature range of 100 °C-400 °C. The application of plasma can provide the advantage of acceptable growth rates and improved material properties like high film density as well as low impurity content at lower deposition temperatures. Also, previously, it has been demonstrated that usage of the metalorganic precursor $(^tBuN)_2(Me_2N)_2W$ along with N_2, H_2/N_2 and NH_3 plasmas for a WN_x ALD process have resulted in very low levels of carbon impurities (<2 at.%).[32] Here, we provide a detailed study on the tungsten trioxide ALD process and the material properties of the as-deposited material. The influence of deposition temperature on GPC, chemical composition, stoichiometry and optical properties of the resulting WO_3 films is investigated.

II. EXPERIMENTAL

In this section, the process conditions for film deposition are discussed followed by a description of the techniques used to characterize the deposited film and related equipment used.

A. Film deposition

WO_3 thin films were deposited in a FlexAL ALD reactor from Oxford Instruments, equipped with an inductively coupled plasma (ICP) source. The reaction chamber is equipped with a turbomolecular pump which enables to reach a base pressure of ~10^{-6} Torr. A detailed description of the ALD reactor can be found in an earlier work of the group.[33] Prior to deposition, the reactor walls were pre-conditioned with 300 ALD cycles of Al_2O_3 and 300 ALD cycles of WO_3 itself. All depositions were performed on c-

Si substrates (2 cm×2 cm) with a thin native oxide layer (~1.5 nm) unless mentioned otherwise. The starting substrates were subjected to an O_2 plasma pre-treatment (10 s) in the ALD reactor in order to remove any surface contamination using the same plasma conditions as during deposition.

TABLE I. Overview of process parameters for the plasma-enhanced ALD of WO_3 from $(^tBuN)_2(Me_2N)_2W$ and O_2 plasma.

Deposition temperature	100-400°C
Chamber wall temperature	100-120°C
Bubbler temperature	50°C
Precursor line temperature	70°C
Chamber base pressure	10^{-6} Torr
Pressure during precursor dosing	30 mTorr
Pressure during co-reactant exposure	15 mTorr
Precursor dosing	3 s
Precursor purge time	5 s
Pre-plasma time	2 s
Co-reactant O_2 plasma exposure	3 s
Co-reactant purge time	5 s
O_2 plasma power	250 W

Table I summarizes the utilized processing conditions. Depositions were performed at different temperatures by varying the set-point temperature of the substrate table from 100 °C-400 °C. The reaction chamber wall temperature was set to 120 °C for all deposition temperatures except for depositions at 100 °C for which the wall temperature

was set to 100 °C as well. The liquid precursor $(^tBuN)_2(Me_2N)_2W$ (99% purity, Sigma Aldrich) was stored in a bubbler maintained at 50 °C and was bubbled into the reaction chamber using Ar (100 sccm) as a carrier gas to enhance precursor delivery. The precursor delivery line to the reaction chamber was heated to 70 °C to prevent any possible precursor condensation.

A standard ALD recipe (Table I) was utilized to perform depositions in this work unless mentioned otherwise. The saturated precursor dosing was fixed at 3 s and a chamber pressure of 30 mTorr was maintained during the precursor dosing step. A pre-plasma time of 2 s was used to stabilize the O_2 gas flow into the ICP source. The saturated co-reactant O_2 plasma exposure was fixed at 3 s. The plasma power was fixed at 250 W and a chamber pressure of 15 mTorr was maintained during the plasma exposure step. After the respective ALD half cycle, Ar gas (100 sccm) was used to purge the reaction chamber for 5 s resulting in a chamber pressure of 30 mTorr.

B. Film analysis

In-situ spectroscopic ellipsometry (SE) was used to monitor the growth of ALD WO_3 films using a rotating compensator ellipsometer (RCE) of type M2000U from J.A. Woollam, Inc. Ellipsometric spectra were recorded after every 10 ALD cycles in the high accuracy mode over a wavelength range of 245 nm-1000 nm. An optical stack model was used to translate the raw ellipsometric spectra into film thickness and optical parameters (n, k) by utilizing the CompleteEASE software. The optical stack model (from bottom to top) consisted of a (1) Si substrate modelled by Si Temp JAW (Temp Library) material model, (2) ~1.5 nm native oxide modelled by NTVE_JAW material model, and (3) a WO_3 layer whose dielectric functions were parameterized by using the Tauc-Lorentz

oscillator. The thickness and optical constants of the WO_3 layer were obtained using the following fitting methodology: In the recorded SE spectral range (245 nm-1000 nm), tungsten oxide films are transparent for wavelengths from 400 nm to 1000 nm and thus, a Cauchy dispersion equation was used to extract the thicknesses of the respective films in this range. Using these thickness values, the optical constants were then determined by using the B-spline material model over the entire recorded SE spectra (245 nm-1000 nm). For this fitting, a bandgap of ~3.1 eV[34,35] was assumed and an initial value of 2.1 was chosen for refractive index which was obtained from the Cauchy dispersion model at the largest wavelength (1000 nm). Subsequently, the optical constants were parameterized using the Tauc-Lorentz oscillator.

To investigate the chemical composition of the as-deposited films, X-ray photoelectron spectroscopy (XPS) was performed using a Thermo Scientific KA1066 spectrometer with a monochromatic Al Kα X-rays having an energy of 1486.6 eV. Also, Rutherford backscattering spectrometry (RBS) and elastic recoil detection (ERD) measurements were done to determine the composition, stoichiometry and mass density. The RBS and ERD measurements were done by Detect 99 B.V Eindhoven, The Netherlands, using a 1.9M eV He^+ beam. The respective areal densities of the constituent elements were determined by simulations. To investigate the crystallinity and crystal structure, grazing incidence X-ray diffraction (GI-XRD) measurements were performed using a PANalytical X'Pert Pro MRD system which utilized a Cu Kα X-ray source (λ=1.54 Å).

III. RESULTS AND DISCUSSION

A. Film growth and uniformity

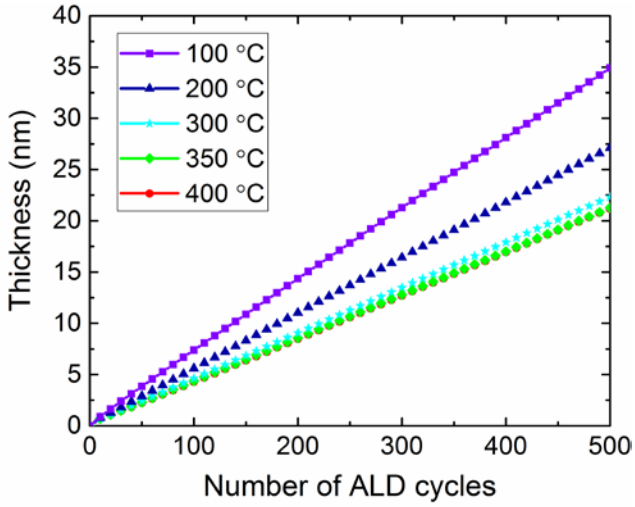

FIG. 1. WO_3 film thickness in progression of number of ALD cycles for deposition temperatures ranging from 100 °C-400 °C, as-determined by in-situ SE

Figure 1 shows the WO_3 film thickness as a function of number of ALD cycles for the investigated deposition temperatures as-determined by in-situ SE. For all temperatures, 500 ALD cycles were performed on the starting substrates. As seen from Fig. 1, the thickness incremented linearly with number of ALD cycles for all temperatures without any nucleation delay. This thickness increment decreased with increasing temperature in the investigated temperature range (100 °C-400 °C). Figure 2(a) and 2(b) show the saturation curves for the precursor dosing and plasma exposure steps, respectively, for various temperatures (100 °C, 300 °C, and 400 °C). For the precursor saturation curves (Fig. 2a), the O_2 plasma exposure time was fixed at 4 s while

varying the precursor dosing and for the O_2 plasma saturation curves (Fig. 2b), the precursor dosing time was fixed at 4 s while varying the O_2 plasma exposure. ALD saturating behaviour was observed over the entire temperature range for both precursor and plasma half-cycles. Also, a decrease in GPC with increasing temperature was observed for both the half-reaction steps.

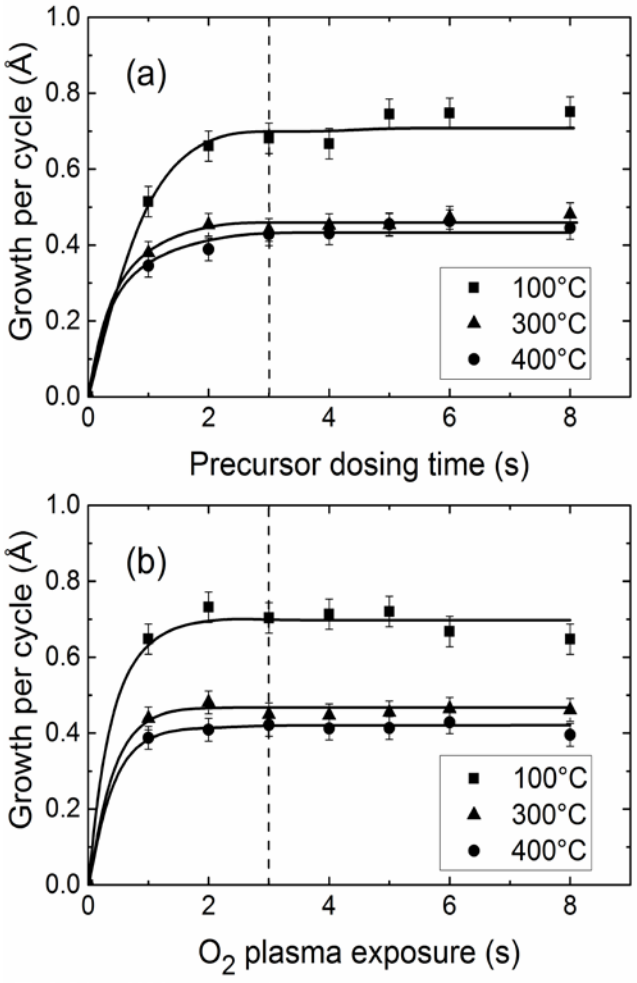

FIG. 2. Saturation curves: GPC as a function of (a) precursor dosing and (b) plasma exposure, for deposition temperatures of 100 °C, 300 °C, and 400 °C. The dotted lines indicate the respective chosen precursor/O_2 plasma saturation times (3s) for the WO_3 ALD process. The solid lines serve as guide to the eye.

In Fig.2a, the GPC was already in the region of saturation for a corresponding precursor dosing time of 3 s independent of temperature. For the O_2 plasma saturation in Fig. 2b, the GPC also exhibited a saturating behaviour starting from 3 s for all investigated temperatures. A small non-ideal component was observed at 100 °C for longer (≥5 s) precursor doses (Fig. 2a) and O_2 plasma exposure times (Fig. 2b).

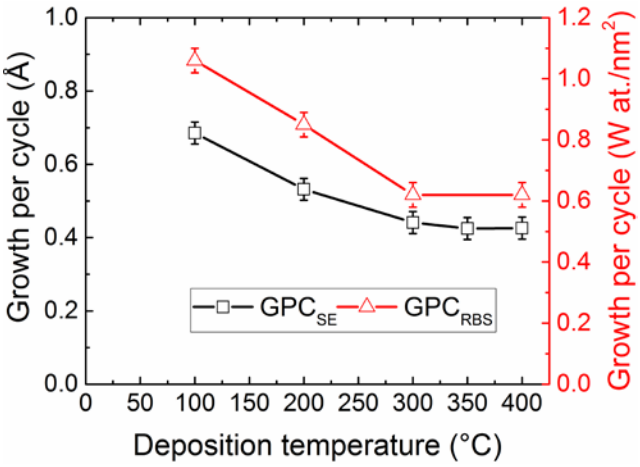

FIG. 3. Growth per cycle (GPC) in terms of (1) thickness: as-determined by in-situ SE (GPC_{SE} - left axis) and (2) deposited W atoms/nm^2: as determined by ex-situ RBS (GPC_{RBS} - right axis), for the investigated deposition temperatures. GPC_{SE} (squares) was calculated by averaging the respective slopes in Fig.1, for the last 100 out of 500 ALD cycles. GPC_{RBS} (triangles) was calculated by dividing the total W atoms/nm^2 by the total number of ALD cycles.

Figure 3 compares the GPC in terms of (1) thickness: as-determined by in-situ SE (GPC_{SE} - left axis) and (2) number of W atoms/nm^2: as-determined by RBS (GPC_{RBS} - right axis), for the investigated deposition temperatures. The GPC_{SE} (squares) was calculated by taking the average of the respective slopes for the last 100 out of 500 ALD cycles in Fig. 1. As seen in Fig. 3, GPC decreased significantly from ~0.7 Å at 100 °C to

~0.45 Å at 300 °C and then stabilized at ~0.45 Å for higher temperatures. Samples with thickness of ~20 nm were utilized for RBS measurements. GPC_{RBS} (triangles) was calculated by dividing the total number of deposited W atoms/nm^2 by the total number of ALD cycles. As seen from Fig. 3, GPC_{RBS} decreased from ~1 W at/nm^2 at 100 °C to ~0.6 W at/nm^2 at 300 °C and then stabilized at ~ 0.6 W at/nm^2 for higher temperatures, which is analogous to the trend exhibited by GPC_{SE}. Similar results have been reported for O_2 plasma-enhanced ALD processes for Al_2O_3[36,37,38] as well as SiO_2[39,40] (utilizing metalorganic precursors) where the decrease in GPC with temperature have been attributed to a reduction of –OH surface reactive groups due to thermally activated dehydroxylation reactions. These processes reported in literature are similar to our WO_3 ALD process and the GPC decrement with temperature from 100 °C to 300 °C in our case can also be due to surface dehydroxylation. The GPC stabilization at temperatures above 300 °C can be a combined effect of reduced –OH surface reactive group density[40] and a transition towards polycrystalline growth which is shown later in the GI-XRD diffractogram (Fig. 7).

For low deposition temperatures (≤200 °C), the observed GPC values are higher than the GPC values reported in literature. For instance, Malm *et al.* and Nandi *et al.* have reported a GPC of ~0.2 Å at around 200 °C using the hexacarbonyl $W(CO)_6$ precursor, which is lower than the observed GPC value of ~0.55 Å in our case.[27,28] The observed GPC values are also higher compared to the process developed by *Liu et al.* who have reported GPC values of <0.2 Å using the same precursor $(^tBuN)_2(Me_2N)_2W$ and H_2O for temperatures below 300 °C.[8] The utilization of O_2 plasma as co-reactant could be the primary reason for the reasonably higher GPC in our process.

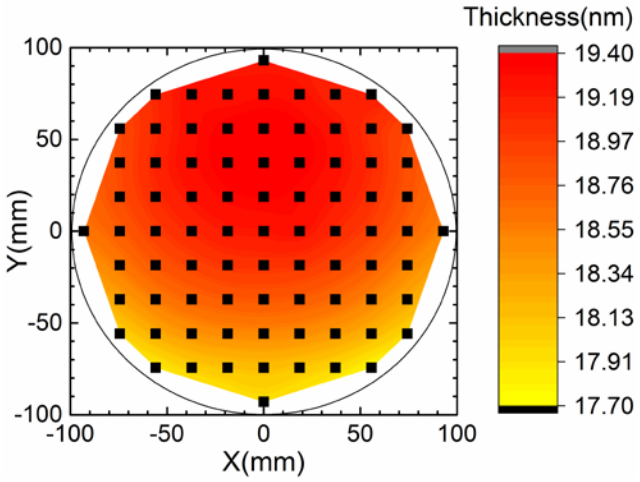

FIG. 4. Thickness uniformity of the WO_3 film on an 8 inch (200 mm) Si wafer as-determined by room temperature SE mapping. The WO_3 film was deposited at 200 °C

Figure 4 shows the WO_3 thickness uniformity on an 8 inch (200 mm) Si wafer evaluated by mapping the thickness over the whole wafer area as-determined by SE at room temperature. For this experiment, 350 WO_3 ALD cycles were performed on the 8 inch Si wafer at 200 °C with a corresponding GPC of ~0.55 Å. The thickness non-uniformity determined by dividing the standard deviation (σ) by the average mean WO_3 thickness, was less than 2.5%. This indicates very good thickness uniformity and the developed WO_3 plasma-enhanced ALD process can potentially be a viable technique for the growth of WO_3 films on large area substrates.

B. Film characterization

The WO_3 films of ~20 nm in thickness which were deposited at various temperatures (100°C-400 °C) were used to study the film properties including chemical composition, optical properties, and crystallinity.

TABLE II. Important film properties of WO_3 including (1) GPC determined by in-situ SE, (2) GPC determined by number of deposited W at.nm^{-2}cycle^{-1}, (3) O/W ratio as well as (4) mass density determined by RBS, and (5) H content determined by ERD measurements, for various deposition temperatures. C and N impurity content in the as-deposited films (bulk) were below the RBS detection limit of 3 and 2 at.%, respectively. The error margins for the respective parameter are indicated along with the first value in each column. No RBS/ERD measurements were performed on the samples deposited at 350 °C.

Deposition temperature (°C)	GPC (Å)	W (at.nm^{-2} cycle^{-1})	O/W	[H] (at.%)	Mass density (gcm^{-3})
100	0.68±0.03	1.06±0.08	2.9±0.1	11.3±0.8	5.8±0.1
200	0.53	0.85	2.9	2.5	5.9
300	0.44	0.62	2.9	2.5	5.9
350	0.43	--	--	--	--
400	0.43	0.62	2.9	6.2	5.9

Table II lists the O/W ratio and H content in the as-deposited WO_3 films, deduced from RBS and ERD measurements respectively, for various deposition temperatures. Typically, tungsten oxide thin films tend to grow sub-stoichiometrically and the level of oxygen deficiency depends on the type of preparation as well as process conditions.[41] In our case, the O/W ratio was found to be constant at 2.9 for all investigated temperatures. With respect to previous WO_3 ALD reports, the O/W ratio of 2.9 is comparable to values (i.e., ~3) reported by Marim *et al.*[27] and is relatively higher than the value (i.e., 2.4) reported by Song *et al.*[16] The effect of the ambient on the film stoichiometry cannot be

ruled out as the samples were stored in air prior to RBS/ERD measurements. The H content in as-deposited films decreased from ~11 at.% at 100 °C to ~2.5 at.% at 300 °C and then increased to ~6 at.% at 400 °C. This H content in the films can originate from the ligands of the precursor (a single precursor molecule has 30 H atoms) and/or from the residual water in the ALD reactor and/or from exposure to the ambient.

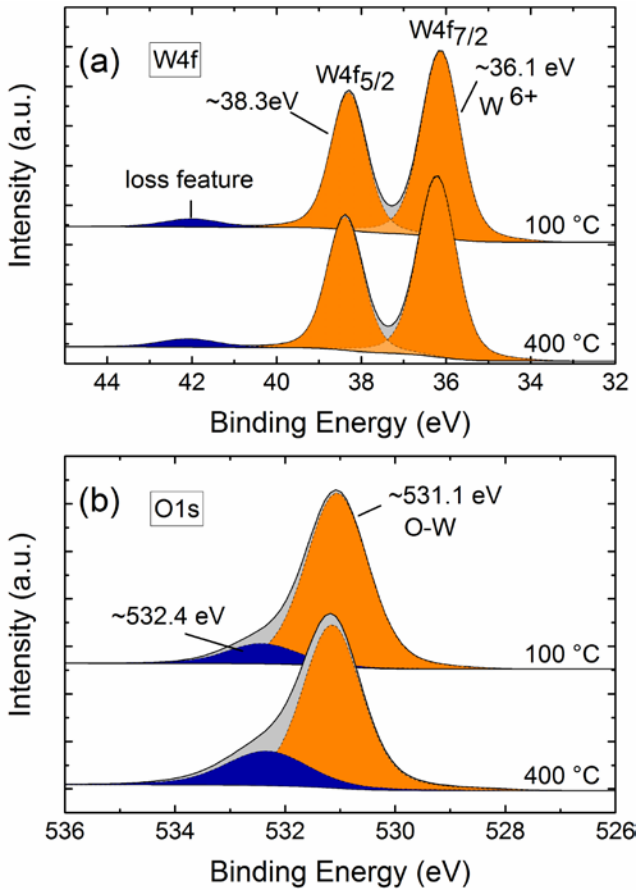

FIG. 5. XPS spectra of WO_3 films deposited at 100 and 400 °C. (a) W4f peaks - fitted W4f core level spectra involving a doublet (orange) and a loss feature (blue). A $W4f_{7/2}$ peak at ~36.1 eV and a $Wf_{5/2}$ peak at ~38.3 eV constituted the doublet. (b) O1s peaks - fitted O1s core level spectra which includes a peak at ~531 eV corresponding to the valency of W^{6+} and another peak at ~532.5 eV which might correspond to residual water adsorbed on the surface.

The mass density of the WO_3 films were deduced from RBS/ERD measurements in conjunction with the WO_3 layer thickness determined from in-situ SE measurements. The mass density was found to be ~5.9 g/cm^3 throughout the deposition range (100 °C-400 °C), which is lower than the bulk density of WO_3 (7.16 g/cm^3). The C and N impurity concentration in the bulk of the films was lower than the RBS detection limit of 3 and 2 at.%, respectively, suggesting a relatively high purity of the as-deposited films.

Figure 5a shows the W4f core level spectra of as-deposited WO_3 films (at 100 °C and 400 °C) acquired by XPS measurements. The measured spectrum was deconvoluted into a doublet (orange) and a loss feature (blue). The doublet comprised of a $W4f_{7/2}$ peak at ~36.1 eV and a $W4f_{5/2}$ peak at ~38.28 eV, with the peaks having an intensity ratio of 0.75 as well as a difference of ~2.17 eV in their binding energies, which corresponds to the W^{6+} oxidation state.[41,42] The O1s XPS spectra (Fig. 5b.) comprised of 2 peaks: one at ~531.1 eV, which can be assigned to O bound to W atoms and a smaller peak at ~532.4 eV, which might originate from O-H bonds or residual water adsorbed on the sample surface.[18] C as well as N were present on the surface and their concentration was reduced to negligible amounts upon depth profiling, which involves sputtering of the sample with Ar^+ ions. Depth profile measurements for W as well as O spectra resulted in reduction of W^{6+} to lower oxidation states due to preferential sputtering of O atoms. Therefore, the spectra in Fig. 5 were acquired prior to sputtering to assess the chemical state correctly.

Figure 6 compares the (a) dispersion of the refractive index *n* and (b) extinction coefficient *k*, of the WO_3 films for various deposition temperatures (100 °C-400 °C). The respective *n* and *k* values were determined through SE measurements using the optical model described in the experimental section. As seen in Fig. 6a, the refractive index

varied between 2.05-2.95 over the spectral range of 1.2-5 eV. For illustration, the refractive indices at a photon energy of 1.96 eV are listed in Table III for various deposition temperatures. As seen from Table III, the refractive index increased from ~2.1 at 100 °C to ~2.28 for ≥300 °C. These values are in good agreement with refractive index values reported for WO_3 in literature.[43,44]

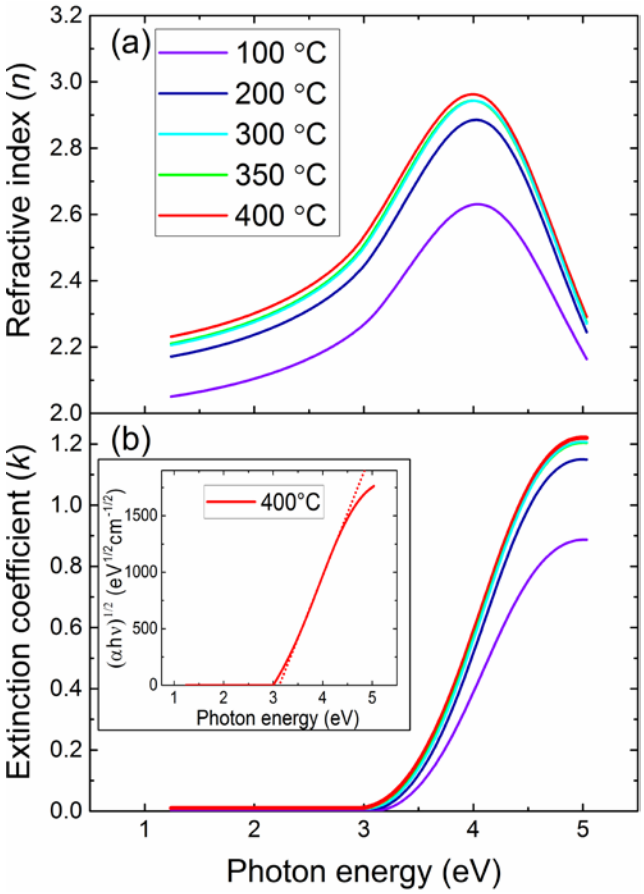

FIG. 6. In-situ SE determined (a) refractive index (*n*) and (b) extinction coefficient (*k*) spectra, of the WO_3 films deposited over the temperature of 100 °C-400 °C. The inset in figure (b) shows the Tauc-plot for the film deposited at 400 °C. The dotted line in the inset indicates the extrapolated linear fit.

The extinction coefficient (Fig. 6b) was zero up to ~3.0 eV and then increased towards the absorption edge. This increase in absorption can be attributed to the electronic transitions between the valence and conduction band, related to the bandgap. The absorption can be mathematically expressed by the Tauc relation:

$$\alpha h\nu \sim (h\nu - E_g)^n \qquad (1)$$

where α is the absorption coefficient, $h\nu$ is the incident energy of photons, E_g is the optical bad gap, and the exponent n which is related to the type of band-gap transition. Typically, n= 1/2, 3/2, 2, and 3 for transitions corresponding to direct allowed, direct forbidden, indirect allowed, and indirect forbidden, respectively.[2,45.] Assuming an indirect transition,[41,43,46] the band gap for WO_3 can be evaluated by extrapolating the linear part of the Tauc plot ($(\alpha h\nu)^{1/2}$ vs. $h\nu$) as shown in Fig. 6b inset. The band gap determined using this procedure are listed in Table III for various deposition temperatures. (Note: The absorption coefficient 'α' was determined from SE measurements.).

TABLE III. SE determined refractive index n and band gap of the WO_3 films deposited at various temperatures. The refractive index is reported at a corresponding photon energy of 1.96 eV.

Deposition temperature (°C)	Refractive index (n)	Band gap (eV)
100	2.10±0.03	3.23±0.04
200	2.22	3.17
300	2.27	3.15
350	2.27	3.13
400	2.28	3.12

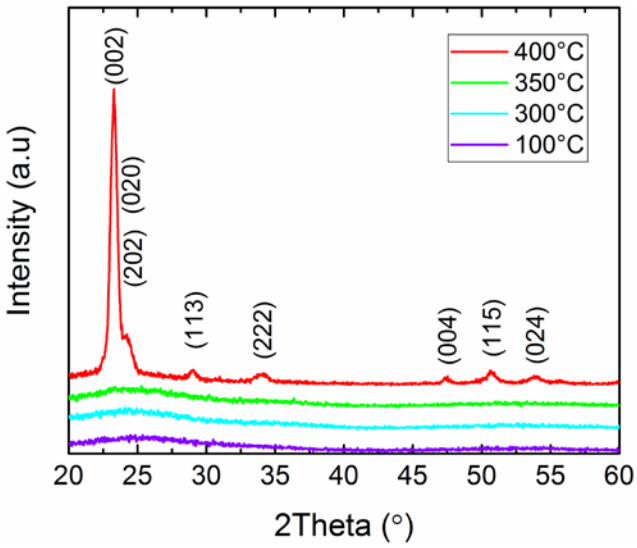

FIG. 7. GI-XRD diffractogram of the WO_3 films deposited at various temperatures. For the WO_3 film deposited at 400 °C, the respective peaks are indexed according to monoclinic WO_3.

The observed bandgap values (3.12 eV-3.23 eV) are in agreement with literature values for WO_3 films.[41,43,45] With respect to deposition temperature, the bandgap decreased marginally from ~3.23 eV at 100 °C to ~3.12 eV for ≥350 °C.

Figure 7 shows the GI-XRD spectra of the as-deposited films at 100 °C, 300 °C, 350 °C, and 400 °C. The GI-XRD diffractogram of the films deposited at 100 °C, 300 °C and 350 °C were featureless. This suggested that the respective films were amorphous. The presence of multiple peaks at 400 °C suggested the growth of a polycrystalline film and the respective peaks could be indexed according to monoclinic WO_3.[8,47] This transition from amorphous to polycrystalline film growth could also explain change in the temperature trend of the GPC from 300 °C to 400 °C (Fig. 3).

IV. SUMMARY and CONCLUSIONS

A new ALD process for WO_3 has been developed using $(^tBuN)_2(Me_2N)_2W$ and O_2 plasma over a wide temperature range of 100 °C-400 °C. The influence of deposition temperature on the film growth as well as film properties has been studied in detail. The application of oxygen plasma, judicious optimization of process conditions, and the right choice of precursor enabled us to develop a new WO_3 ALD process characterized by (1) a relatively high GPC with very good uniformity, (2) low impurity incorporation, (3) wide temperature window, and (4) near stoichiometric film composition. Due to the relatively high purity of the films and the capability to deposit at low temperatures, the presented process is likely to be suitable for many applications including electrochromic displays, solar cells and synthesis of 2D-WS_2.

ACKNOWLEDGMENTS

The authors acknowledge Jeroen van Gerwen and Cristian van Helvoirt for their technical assistance, Martijn Vos as well as Tahsin Faraz for their valuable suggestions, and Aileen Omahony from Oxford Instruments for her assistance in uniformity measurements. This work has been supported by the European Research Council (grant agreement number: 648787).

[1] C.G. Granqvist, in *Handbook of Inorganic Electrochromic Materials* 19–27 (Elsevier, 1995).

[2] C.G. Granqvist, *Sol. Energy Mater. Sol. Cells* **60,** 201–262 (2000).

[3] S. Balaji, Y. Djaoued, A.-S. Albert, R.Z. Ferguson and R. Brüning, *Chem. Mater.* **21,** 1381–1389 (2009).

[4] C. Yan, W. Kang, J. Wang, M. Cui, X. Wang, C.Y. Foo, K.J. Chee and P.S. Lee, *ACS Nano* **8,** 316–322 (2014).

[5] J. Polleux, A. Gurlo, N. Barsan, U. Weimar, M. Antonietti and M. Niederberger, *Angew. Chemie - Int. Ed.* **45,** 261–265 (2006).

[6] C. Balázsi, L. Wang, E.O. Zayim, I.M. Szilágyi, K. Sedlacková, J. Pfeifer, A.L. Tóth and P.-I. Gouma, *J. Eur. Ceram. Soc.* **28,** 913–917 (2008).

[7] Z.-G. Zhao and M. Miyauchi, *Angew. Chemie Int. Ed.* **47,** 7051–7055 (2008).

[8] R. Liu, Y. Lin, L.-Y. Chou, S.W. Sheehan, W. He, F. Zhang, H.J.M. Hou and D. Wang, *Angew. Chemie Int. Ed.* **50,** 499–502 (2011).

[9] C.M. Lampert, *Sol. Energy Mater. Sol. Cells* **76,** 489–499 (2003).

[10] D.R. Rosseinsky and R.J. Mortimer, *Adv. Mater.* **13,** 783–793 (2001).

[11] http://www.hwnanomaterial.com

[12] M. Bivour, J. Temmler, H. Steinkemper and M. Hermle, *Sol. Energy Mater. Sol. Cells* **142,** 34–41 (2015).

[13] L.G. Gerling, S. Mahato, A. Morales-Vilches, G. Masmitja, P. Ortega, C. Voz, R. Alcubilla and J. Puigdollers, *Sol. Energy Mater. Sol. Cells* **145,** 109–115 (2016).

[14] M. Mews, L. Korte and B. Rech, *Sol. Energy Mater. Sol. Cells* **158,** 77–83 (2016).

[15] H.R. Gutiérrez, N. Perea-López, A.L. Elías, A. Berkdemir, B. Wang, R. Lv, F. López-Urías, V.H. Crespi, H. Terrones and M. Terrones, *Nano Lett.* **13,** 3447–3454 (2013).

[16] J. Song, J. Park, W. Lee, T. Choi, H. Jung, C.W. Lee, S. Hwang, J.M. Myoung, J. Jung, S.-H. Kim, C. Lansalot-Matras and H. Kim, *ACS Nano* **7,** 11333–11340 (2013).

[17] A. Azens, M. Kitenbergs and U. Kanders, *Vacuum* **46,** 745–747 (1995).

[18] Y. Baek and K. Yong, *J. Phys. Chem. C* **111,** 1213–1218 (2007).

[19] H.S. Witham, P. Chindaudom, I. An, R.W. Collins, R. Messier and K. Vedam, *J. Vac. Sci. Technol. A Vacuum, Surfaces, Film.* **11,** 1881–1887 (1993).

[20] R.S. Vemuri, M.H. Engelhard and C.V. Ramana, *ACS Appl. Mater. Interfaces* **4,** 1371–1377 (2012).

[21] P. Judeinstein and J. Livage, *J. Mater. Chem.* **1,** 621–627 (1991).

[22] A. Cremonesi, D. Bersani, P.P. Lottici, Y. Djaoued and P.V. Ashrit, *J. Non. Cryst. Solids* **345–346,** 500–504 (2004).

[23] R.U. Kirss and L. Meda, *Appl. Organomet. Chem.* **12,** 155–160 (1998).

[24] R.G. Gordon, S. Barry, J.T. Barton and R.N.R. Broomhall-Dillard, *Thin Solid Films* **392,** 231–235 (2001).

[25] P. Tägtström, P. Martensson, U. Jansson and J.-O. Carlsson, *J. Electrochem. Soc.* **146,** 3139 (1999).

[26] Dezelah, O.M. El-Kadri, I.M. Szilágyi, J.M. Campbell, K. Arstila, L. Niinistö and C.H. Winter, *J. Am. Chem. Soc.* **128,** 9638–9639 (2006).

[27] J. Malm, T. Sajavaara and M. Karppinen, *Chem. Vap. Depos.* **18,** 245–248 (2012).

[28] D.K. Nandi and S.K. Sarkar, *Energy Procedia* **54,** 782–788 (2014).

[29] M.A. Mamun, K. Zhang, H. Baumgart and A.A. Elmustafa, *ECS J. Solid State Sci. Technol.* **4,** P398–P401 (2015).

[30] K. Zhang, C. McCleese, P. Lin, X. Chen, M. Morales, W. Cao, F.J. Seo, C. Burda and H. Baumgart, *ECS Trans.* **69,** 199–209 (2015).

[31] N. Li, L. Feng, J. Su, W. Zeng and Z. Liu, *RSC Adv.* **6,** 64879–64884 (2016).

[32] M.J. Sowa, Y. Yemane, J. Zhang, J.C. Palmstrom, L. Ju, N.C. Strandwitz, F.B. Prinz and J. Provine, *J. Vac. Sci. Technol. A Vacuum, Surfaces, Film.* **35,** 01B143 (2017).

[33] H.C.M. Knoops, E.M.J. Braeken, K. de Peuter, S.E. Potts, S. Haukka, V. Pore and W.M.M. Kessels, *ACS Appl. Mater. Interfaces* **7,** 19857–19862 (2015).

[34] A. Subrahmanyam and A. Karuppasamy, *Sol. Energy Mater. Sol. Cells* **91,** 266–274 (2007).

[35] I. Valyukh, S. Green, H. Arwin, G.A. Niklasson, E. Wäckelgård and C.G. Granqvist, *Sol. Energy Mater. Sol. Cells* **94,** 724–732 (2010).

[36] E. Langereis, J. Keijmel, M.C.M. van de Sanden and W.M.M. Kessels, *Appl. Phys. Lett.* **92,** 231904 (2008).

[37] S.E. Potts, W. Keuning, E. Langereis, G. Dingemans, M.C.M. van de Sanden and W.M.M. Kessels, *J. Electrochem. Soc.* **157,** P66 (2010).

[38] G. Dingemans, M.C.M. van de Sanden and W.M.M. Kessels, *Electrochem. Solid-State Lett.* **13,** H76 (2010).

[39] G. Dingemans, C.A.A. van Helvoirt, D. Pierreux, W. Keuning and W.M.M. Kessels, *J. Electrochem. Soc.* **159,** H277–H285 (2012).

[40] S.E. Potts and W.M.M. Kessels, *Coord. Chem. Rev.* **257,** 3254–3270 (2013).

[41] D. Gogova, K. Gesheva, A. Szekeres and M. Sendova-Vassileva, *Phys. status solidi* **176,** 969–984 (1999).

[42] C.G. Granqvist, in *Handbook of Inorganic Electrochromic Materials* 111–137 (1995).

[43] K. Muthu Karuppasamy and A. Subrahmanyam, *J. Phys. D. Appl. Phys.* **42,** 95301 (2009).

[44] H. Camirand, B. Baloukas, J.E. Klemberg-Sapieha and L. Martinu, *Sol. Energy Mater. Sol. Cells* **140,** 77–85 (2015).

[45] S.M.A. Durrani, E.E. Khawaja, M.A. Salim, M.F. Al-Kuhaili and A.M. Al-Shukri, *Sol. Energy Mater. Sol. Cells* **71,** 313–325 (2002).

[46] R.A. May, L. Kondrachova, B.P. Hahn and K.J. Stevenson, *J. Phys. Chem. C* **111,** 18251–18257 (2007).

[47] S. Tanisaki, *J. Phys. Soc. Japan* **15,** 573–581 (1960).